ADVANCED ENERGY MATERIALS
www.advenergymat.de

Use of Interplay between A-Site Non-Stoichiometry and Hydroxide Doping to Deliver Novel Proton-Conducting Perovskite Oxides

*Jin Goo Lee, Aaron B. Naden, Cristian D. Savaniu, Paul A. Connor, Julia L. Payne, Jonathan M. Skelton, Alexandra S. Gibbs, Jianing Hui, Stephen C. Parker, and John T. S. Irvine**

The magnitude of ionic conductivity is known to depend upon both mobility and number of available carriers. For proton conductors, hydration is a key factor in determining the charge–carrier concentration in ABO_3 perovskite oxides. Despite the high reported proton mobility of calcium titanate ($CaTiO_3$), this titanate perovskite has thus far been regarded as a poor proton conductor due to the low hydration capability. Here, the enhanced proton conductivity of the defective calcium titanate $Ca_{0.92}TiO_{2.84}(OH)_{0.16}$ prepared by replacing lattice oxygens with hydroxyl groups via a solvothermal route is shown. Conductivity measurements in a humidified Ar atmosphere reveal that, remarkably, this material exhibits one order of magnitude higher bulk conductivity (10^{-4} S cm^{-1} at 200 °C) than hydrated stoichiometric $CaTiO_3$ prepared by traditional solid-state synthesis due to the higher concentration of protonic defects and variation in the crystal structure. The replacement of Ca^{2+} by Ni^{2+} in the $Ca_{1-x}Ti_1O_{3-2x}(OH)_{2x}$, which mostly exsolve metallic Ni nanoparticles along orthorhombic (100) planes upon reduction, is also demonstrated. These results suggest a new strategy by tailoring the defect chemistry via hydration or cation doping followed by exsolution for targeted energy applications.

1. Introduction

Perovskite oxides (ABO_3) have been studied for a number of energy applications including proton conductors, batteries, photocatalysis, and fuel/electrolysis cells due to the favorable properties that can be achieved by controlling the defect chemistry.[1–16]

Some perovskite oxides such as barium cerate ($BaCeO_3$) exhibit good proton conductivity under humidified atmosphere through the Grotthuss mechanism whereby excess proton or protonic defect diffuses between oxygen sites.[1–4] The process is initiated by incorporation of hydroxyl groups ($OH^{\bullet}$ protonic defects) at oxygen vacancy sites ($V_O^{\bullet\bullet}$) (Equation (1)), illustrated in Kröger–Vink notation as:

$$H_2O + V_O^{\bullet\bullet} + O_O^x \rightleftarrows 2OH_O^{\bullet} \quad (1)$$

In materials such as $BaCeO_3$, where the B-site cations are in the +4-oxidation state, substitution of trivalent transition metal ions creates additional $V_O^{\bullet\bullet}$ and allows for a larger degree of hydration and higher concentration of H^+ charge carriers. For example, $Ba(Ce,Zr)_{1-x}Y_xO_{3-\delta}$ (BCZY) has shown high proton conductivity ($\approx 10^{-2}$ S cm^{-1} at 500 °C, $[OH^{\bullet}] \approx 0.1$ for $x = 0.1$) together with good chemical stability in atmospheres containing CO_2.[5–8]

Calcium titanate ($CaTiO_3$) has orthorhombic *Pbnm* structure (a = 5.3796 (1) Å, b = 5.4423(3) Å, c = 7.6401(5) Å, V = 223.68(1) Å^3, ρ = 4.04 g cm^{-3}) and is incipient ferroelectric and diamagnetic.[9] Munch et al. suggested the potential of $CaTiO_3$ as a proton conductor based on a quantum molecular dynamics study, which identified that the much shorter O—O separation of

J. G. Lee, A. B. Naden, C. D. Savaniu, P. A. Connor, J. L. Payne, J. Hui, J. T. S. Irvine
School of Chemistry
University of St Andrews
St Andrews, Fife KY16 9ST, UK
E-mail: jtst@st-andrews.ac.uk

The ORCID identification number(s) for the author(s) of this article can be found under https://doi.org/10.1002/aenm.202101337.

DOI: 10.1002/aenm.202101337

J. G. Lee
Advanced Energy Materials and Components R&D Group
Korea Institute of Industrial Technology
33-1 Jungang-ro, Yangsan, Gyeongsangnam-do 50623, Republic of Korea
J. M. Skelton
Department of Chemistry
University of Manchester
Oxford Road, Manchester M13 9PL, UK
A. S. Gibbs
ISIS Facility
Rutherford Appleton Laboratory
Chilton, Didcot OX11 OQX, UK
S. C. Parker
Department of Chemistry
University of Bath
South Building, Soldier Down Ln, Claverton Down Bath BA2 7AX, UK

$CaTiO_3$ (≈245 pm) and $SrTiO_3$ compared to $BaCeO_3$ (≈280 pm) led to shortening the proton transfer time scale.[10,11] The proton conductivity of Sc-doped $SrTiO_3$ was 10^{-4} S cm^{-1} above 300 °C in $p(H_2O)$≈0.03 atm ($[OH^{\bullet}]$≈0.02 for $SrTi_{0.98}Sc_{0.02}O_3$).[4,17] Waser also reported high protonic defect solubility in $BaTiO_3$.[18] Despite this, $CaTiO_3$ has historically been considered to be a poor proton conductor, hence the absence of any experimental works or data for proton conductivity. Kreuer suggested that a low hydration capability may be responsible for the low proton conductivity of $CaTiO_3$.[1,2] To examine this, we prepared $CaTiO_3$ powders using a conventional solid-state synthesis (denoted "CTO(SS)") together with powders hydrated via a hydrothermal process at 200 °C for 1 day (denoted "hydrated CTO(SS)"). The weight loss of the hydrated CTO(SS) was determined from TGA measurements to be 0.2 wt% ($[OH^{\bullet}]$≈0.015 in $CaTiO_3$), indicating very low water contents, This translates to a poor proton conductivity of $\sigma_{bulk} = 10^{-6}$ S cm^{-1} at 300 °C in wet Ar due to low proton carrier concentrations. (Figure S1, Supporting Information).

2. Results and Discussion

Instead of using the typical strategy of B-site doping to create more $V_O^{\bullet\bullet}$ sites for subsequent hydration, as per Equation 2, the lattice oxygens (O_O^x) were directly replaced with hydroxide (OH^-) via a solvothermal process to enhance hydration capability of $CaTiO_3$. The crystal growth followed by hydrolysis and condensation make it possible to synthesize the hydrated $CaTiO_3$ (denoted as CTO(ST)) with $OH^{\bullet}$, and compensating A-site vacancies as in Equation 3:[19]

$$2B_B^x + O_O^x + M_2O_3 = 2M_B' + V_O^{\bullet\bullet} + 2BO_2 \quad (2)$$

$$ABO_3 + xH_2O = 2xOH_O^{\bullet} + xAO(s) + xV_A'' + (1-x)A_A^x + B_B^x + (3-2x)O_O^x \quad (3)$$

The weight loss of these CTO(ST) was substantially increased to ≈1.9 wt% ($[OH^{\bullet}]$≈0.151 in $CaTiO_3$) in a temperature range from 200 to 600 °C compared to 0.2 wt% ($[OH^{\bullet}]$≈0.015 in $CaTiO_3$) of the hydrated CTO(SS) (**Figure 1**a). An important consequence of this tenfold increase in hydration—with ≈70% recovery of the initial structural OH^- upon rehydration (Figure S2, Supporting Information)—is the possibility of enhanced proton conductivity of CTO(ST) according to the ionic conductivity equation. The final stoichiometry estimated using both energy dispersive X-ray spectroscopy (EDX) and thermogravimetric analyzer (TGA) was

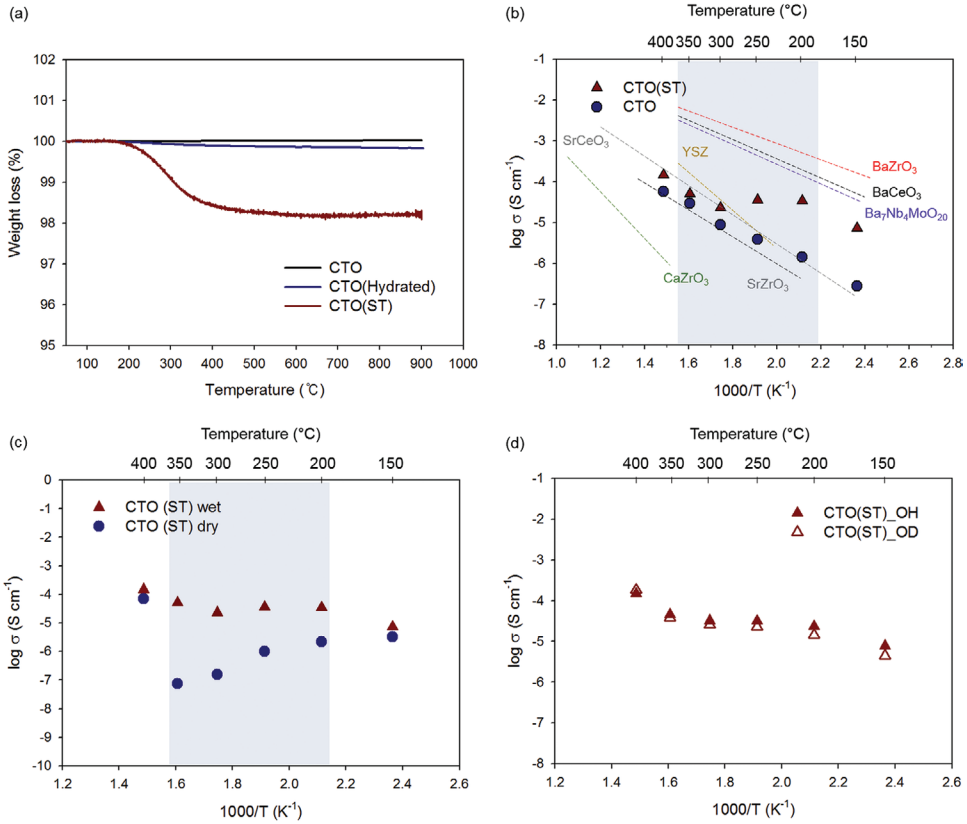

Figure 1. Hydration capabilities and bulk conductivities. a) TGA curves for CTO(SS), hydrated CTO(SS), and CTO(ST) samples in dry air. b) Comparison of the conductivities of CTO(SS) and CTO(ST) samples in wet (humidified) Ar atmosphere (pH_2O ≈ 0.03 atm), with literature data for $BaZrO_3$,[7] $BaCeO_3$,[4] $Ba_7Nb_4MoO_{20}$,[21] $CaZrO_3$,[22] $SrZrO_3$,[7] and $SrCeO_3$.[23] All of the perovskites that are used for comparison, for example, $BaZrO_3$, are acceptor doped. c) Bulk conductivities of CTO(ST) in dry (pH_2O<10^{-6} atm) and wet (pH_2O ≈ 0.03 atm) Ar atmospheres. The shaded box indicates the range of temperatures over which weight loss is observed in TGA analyses. d) Bulk conductivities of CTO(ST)_OH and CTO(ST)_OD in a flow of N_2 gas through H_2O and D_2O, respectively. The difference of the conductivities between CTO(ST)_OH and CTO(ST)_OD is ≈1.6, which corroborates proton conduction is main transport.

found to be $CaTiO_3$ for CTO (SS) and $Ca_{0.92}TiO_{2.84}(OH)_{0.16}$ for CTO(ST): significant lower density supports the presence of A-site vacancies compensated by OH^- in CTO(ST) (see Figures S3 and S4 and Tables S1–S3, Supporting Information, for further information and discussions on powder X-ray diffraction and EDX). The crystal structure of this material was stable up to 900 °C in oxidized and reduced conditions, but lattice parameters were changed due to the hydroxyl ion losses. We expect that it would be stable over 900 °C in both environments (Figure S5, Supporting Information).

To assess the influence of hydration on the proton conductivity, the electrical properties of CTO(SS) and CTO(ST) pellets were measured under dry and humidified Ar atmospheres using AC impedance spectroscopy. These spectra were separated into grain-interior (bulk) and grain-boundary conductivity using an equivalent circuit model (Figures S6–S12, Supporting Information).[20] The Arrhenius plot (Figure 1b) reveals a remarkable increase in the bulk conductivity of CTO(ST) below 300 °C, with an order of magnitude higher conductivity of 3.4×10^{-5} S cm^{-1} at 200 °C compared to 1.4×10^{-6} S cm^{-1} of CTO(SS), being comparable to the benchmark conductivity values obtained for barium zirconate/cerate and disordered hexagonal perovskite, $Ba_7Nb_4MoO_{20}$ at low temperature regime.[4,7,21–23] The plateau from 200 to 300 °C results from a decrease in the concentration of proton charge carriers (n) interlinked with an increase in mobility (μ) of the remaining protons (see Equation S2), which suggests the maximum proton conductivity of CTO(ST) in the humidified atmosphere is a result of successful replacement of the lattice oxygens with hydroxide ions. The conductivity of CTO(ST) in dry Ar reflects the close dependence of proton conductivity on pH_2O (Figure 1c). The significant increase in the conductivity above 350 °C likely results from the development of electronic conduction due to the mildly reducing atmosphere. A reduction in bulk conductivity of the deuterated CTO(ST) (denoted "CTO(ST)_OD") compared to the hydrated CTO(ST) (denoted "CTO(ST)_OH") further support proton conduction of the CTO(ST) due to isotope effects (Figure 1d). Equivalent circuit analysis with electric modulus M″ was used to extract the bulk resistivity in the isotope experiments (Figure S13, Supporting Information).[20] The bulk resistivity in N_2+D_2O is 1.4–1.7 times higher than in N_2+H_2O in 150 to 300 °C, which demonstrates that proton conduction is dominant in the temperature regime (Figure S14, Supporting Information).

Proton conduction is highly sensitive to the crystalline environment of a material. Therefore, to elucidate the origin of the enhanced proton conductivity of CTO(ST), deuterated CTO(SS) and CTO(ST) samples were prepared, and analyzed by high-resolution neutron powder diffraction (HRPD) at ISIS Neutron and Muon Source.[24] As CTO(ST) samples are A-site deficient hydrated perovskites, A-site defects and unit-cell expansion induced by hydration would cause strained structures. Moreover, CTO(ST) is a few hundreds of nanometers in size, and therefore it was difficult to obtain sharp and clear neutron diffraction patterns in our experiments, which is the reason for the worse difference curve in Rietveld refinement. The data obtained from TGA combined with mass spectroscopy clearly shows successful deuteration of the samples with $[OD^\bullet] = 0.157 \pm 0.01$ (Figure S15, Supporting Information). Rietveld refinement (**Figure 2**a,b and Method) for CTO(SS) and CTO(ST) revealed the fractional occupancy of deuterons positioned at the corner of TiO_6 octahedra (O-D: 1.08 Å) was 0.16(1) for CTO(ST) (Figure S16 and Tables S4 and S5, Supporting Information), in agreement with the TGA mass loss. The occupation of the Ca sites refines to ≈92 ± 0.8%, confirming the A-site deficiency compensated by OH^- incorporation. The stoichiometry of the CTO(SS) and CTO(ST) samples determined by Rietveld refinement was $CaTiO_3$ and $Ca_{0.92}TiO_{2.84}(OD)_{0.16}$, respectively. The hydration-induced A-site defects modified the Ti—O bond lengths in the TiO_6 octahedra by shortening of the Ti(1)—O(5,6) bonds aligned along the b-axis (CTO(SS) = 1.9588 Å, CTO(ST) = 1.9490 Å) whereas the Ti(1)—O(1,2) bonds along the c-axis are elongated (CTO(SS) = 1.9519 Å, CTO(ST) = 1.9570 Å) (Figure 2c). The tensile stress due to the c-axis elongation leads to the unit-cell volume expansion and reduced octahedral tilting, which is reflected in the larger Ti(1)—O(2)—Ti(3) and Ti(1)—O(6)—Ti(2) bond angles (CTO(ST)-156.78/157.80°; CTO(SS)-156.27/155.47°) (Figure 2d and Tables S6 and S7, Supporting Information). Munch et al. identified two proton transfer mechanisms in $CaTiO_3$, viz. intra- and inter-proton transfer, which account for 30% and 70% of the conductivity, respectively.[10,11] As inter-proton transfer strongly depends on the octahedral distortion, the reduced octahedral tilting in CTO(ST) is likely to disrupt this mechanism: however, the inter-proton transfer is probably different near the A-site vacancy region as shown in Figure 2e. We anticipate that proton migration might be facilitated near the domain in terms of the nanoscale percolation pathway recently reported by Draber et al.[25] On the other hand, the intra-proton transfer is expected to be fast since the shorter O—O separation (CTO(ST): ≈2.72 Å, CTO(SS): ≈2.76 Å) would facilitate proton transfer to nearest-neighbor oxygen sites along the edges of octahedra (Figure 2e and Table S7, Supporting Information). These results therefore indicate a defect-driven proton transfer mechanism, explaining the high level of proton conduction observed for this sample, in strong agreement with previous studies.[17]

As an extension of this work, we also attempted Ni substitution at Ca-sites in the $Ca_{0.92}TiO_{2.84}(OH)_{0.16}$ sample.[26] This may seem unusual, given that Ni^{2+} widely accepted to be substitute at the Ti sites (B-sites) in titanate perovskites, due to the better match in ionic radius to typical B-site cations compared to large A-site ions (Ba, Sr, Ca). However, the difference between the effective ionic radii of Ni^{2+} (83 pm, CN 6) and Ca^{2+} (134 pm, CN 12) is similar to the difference in the effective radii of Nd^{3+} (98.3 pm) and Ba^{2+} (161 pm), which have been shown to occupy both A- and B-sites of perovskites.[27] Hence this opens up the possibility of Ni substitution for the A-site of perovskites. Computational modelling by Beale et al. suggests Ni^{2+} should preferentially occupy the Sr^{2+} site in $SrTiO_3$, while this contradicts EXAFS measurements,[28] the two findings can be reconciled by considering the kinetics of the particular hydrothermal synthesis methods used to prepare the material. A similar preparation method was also employed in our study. Zhang et al. also observed Pt re-localization at the Ca sites (Pt(IV): 76.5 pm, CN: 6) in Pt-doped $CaTiO_3$ following reoxidation.[29] First-principles modelling using solid-state density-functional theory (see Methods) predicts formation enthalpies (ΔH_F) of 1.68 and 2.46 eV for Ni substitution at the A- and B-sites in $CaTiO_3$, respectively (Table S8, Supporting Information), suggesting that the former is most favourable.

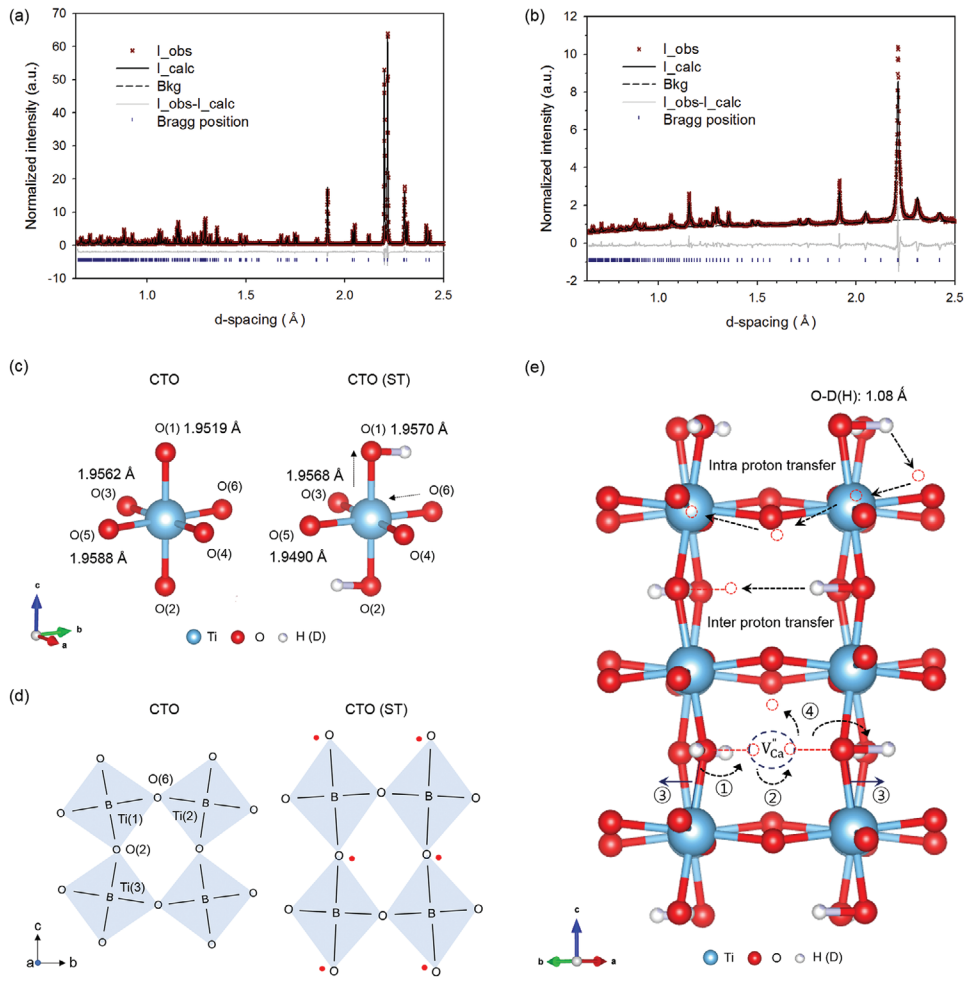

Figure 2. Neutron diffraction analysis of deuterated CTO(SS) and CTO(ST). a) HRPD refinements from powder data collected for CTO(SS) with R_{wp} = 4.53% and GOF = 2.94. b) HRPD refinements from powder data collected for CTO(ST) with R_{wp} = 4.85% and GOF = 3.42. The background seen in the HRPD of CTO(ST) typically results from incoherent scattering from protons. c) Comparison of the Ti—O bond lengths in CTO(SS) and CTO(ST). d) Schematic illustration of the unit-cell volume expansion observed in CTO(ST) compared to CTO(SS). e) Schematic image of suggested proton transfer for CTO(ST). Reduced repulsion between B-site cations and protons (deuterons) bound to O(1,2) along the *c*-axis is expected due to the elongation of the Ti(1)—O(1,2) bond, which may enable fast proton reorientation toward the edge of the octahedra. The protons migrate to neighboring oxygen sites and the shorter O—O distances then facilitate intra-proton transfer to the neighboring sites along the *a*- or *b*-axes. Inter-proton transfer is also possible, but may be slightly weakened due to the reduced octahedral tilting: however, near the A-site vacancy region, protons may be easily rotated to the vacant site (No.1), and transferred to adjacent TiO_6 octahedra (No.2). The proton could escape the vacancy region (No.4) when the O—O distance between the vertices of the octahedra becomes farthest by the oxide lattice vibration (No.3).

We initially expected A-site Ni doping would have negative effects on proton conductivity because it decreases oxygen vacancy concentrations and thus proton concentrations. however, the electrical properties of the Ni doped sample were not that different from the un-doped sample in this experiment (Figure S17, Supporting Information). We think that this is due to similar concentrations of hydroxide ions between un-doped and Ni-doped samples. Controlling stoichiometry is very difficult via solvothermal synthesis at the current stage and therefore, the issue for stoichiometry control should be first addressed to precisely compare not only the effect of Ni doping on electrical properties but also the location of Ni ions in the perovskite structures.

The Rietveld refinement for HRPD data collected from Ni-doped $CaTiO_3$ prepared by solvothermal synthesis (denoted "CNTO(ST)") was used to confirm this (see Methods). The refinement for the Ti sites showed unbalanced site occupation (Ti>1) with higher R_{wp} = 5.64% and goodness of fit (GOF) = 3.96 compared to R_{wp} = 5.40% and GOF = 3.81 for the Ca sites (**Figure 3**a and Tables S9 and S10, Supporting Information), which suggests that Ni^{2+} is more likely to replace Ca^{2+} than Ti^{4+}. Combining the fractional occupancies from Rietveld refinement with both TGA and EDX measurements (Tables S11 and S12, Supporting Information) allowed us to determine the stoichiometry of the CNTO(ST) samples to be $(Ca_{0.87}Ni_{0.03})TiO_{2.80}(OD)_{0.20}$. CNTO(ST) also shows a higher degree of orthorhombic distortion, which may explain the incorporation of smaller Ni^{2+} into Ca^{2+} sites (Figure 3b). The crystal structure shows square-planar coordination of the Ni^{2+} ions in the (010) plane and aligned off-center in the (110) plane (Figure 3c). EXAFS reveals two different Ni—O interatomic distances of 1.895 and 2.187 Å. The

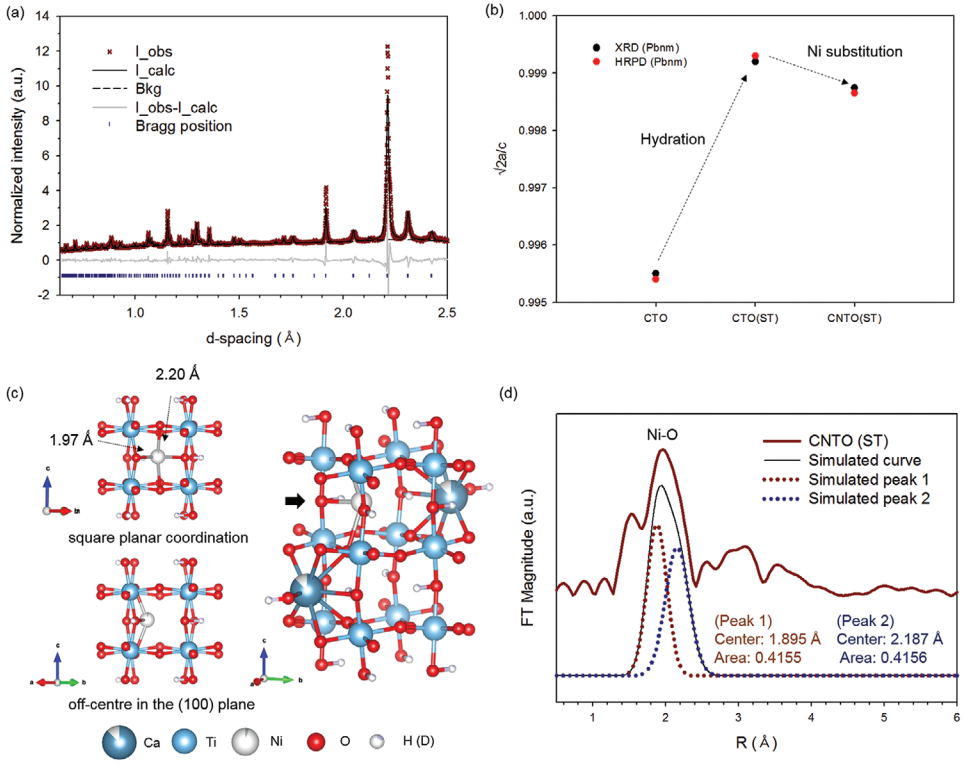

Figure 3. Crystal structure of CNTO(ST) obtained from HRPD and EXAFS measurements. a) HRPD refinements of powder data collected for CNTO(ST) with R_{wp} = 5.40% and GOF = 3.81. b) Orthorhombicity of CNTO(ST) obtained from HRPD refinements. A value of 1 corresponds to an ideal orthorhombic structure, that is, no distortion. c) Crystal structure obtained from neutron diffraction. d) Deconvoluted Ni K-edge EXAFS spectra showing the peak assigned to the two independent Ni—O bond lengths.

Ni—O bond lengths obtained from Rietveld refinement of the neutron data with a model, incorporating Ni^{2+} on the A-site correspond is shown in Figure 3c,d (see Figure S18 and Table S7, Supporting Information).

Metal exsolution from perovskite oxides has attracted significant attention in catalysis due to the homogeneous distribution and strong anchorage of metal nanoparticles obtained at the perovskite surfaces.[30,31] To investigate the characteristics of Ni exsolution from the A-sites of $CaTiO_3$, we heated $(Ca_{0.87}Ni_{0.03})TiO_{2.80}(OH)_{0.20}$ at 700 °C in 5% H_2/Ar for 20 h. The exsolution can be expressed through the following reaction scheme if Ni ions are fully exsolved on the perovskite surfaces in a form of metal nanoparticles:

$$(Ca_{1-x-n}Ni_n)TiO_{3-2x}(OH)_{2x} + \alpha H_2(g) \rightarrow Ca_{1-x-n}TiO_{3-x-n} + nNi_{Ex} + (x+\alpha)H_2O(g) \quad (4)$$

The as-prepared CNTO(ST) is cuboidal in shape with dimensions of ≈500 nm (**Figure 4**a). Initially the cubes present $\{100\}_{pc}$ pseudocubic terminations with sharp edges as in Figure 4a. After reduction, these edges become truncated to smaller $\{110\}_{pc}$ facets decorated with Ni nanoparticles of ≈10–20 nm in size (Figure 4b and Figure S19, Supporting Information). The formation of titanium dioxide-terminated $\{100\}_{pc}$ facets is favored for the as-prepared CNTO(ST) cuboids synthesized via solvothermal routes with alkaline mineralizer, due to strong chemisorption of hydroxyl ions on the surface containing more electronegative Ti ions. This is illustrated by the cross-sectional high-resolution high angle annular dark field (HAADF) image and inset intensity profile in Figure 4c since HAADF contrast increases with increasing atomic number Z.[32] Favorable exsolution of Ni nanoparticles on ABO-terminated $\{110\}_{pc}$ facets involving A-site vacancies (Figure 4d) can therefore be expected due to lower migration repulsion,[31] explaining the preferential localization of the particles to the truncated edges of the cubes in Figure 4b.

Figure 4e,f shows atomic resolution scanning transmission electron microscopy (STEM) images of the perovskite and Ni nanoparticles along with strain maps in Figure 4g–i calculated relative to bulk Ni.[33] Figure 4e shows a representative examples of a nanoparticle emerging from $\{110\}_{pc}$ pseudocubic terraces and viewed along the $<001>_{pc}$ zone axis of the perovskite. As can be seen from Figure 4e, the particle does not show clear lattice fringes at this sample orientation, indicating that there is some rotation between the crystal lattices of the Ni and the perovskite. By tilting the sample toward the Ni zone axis, it is possible to visualize the atomic structure of the nanoparticles, as shown in Figure 4f. This embedded particle shows a much larger orientational mismatch with the perovskite compared to ones formed on $\{100\}_{pc}$ facets (Figure S20, Supporting Information), requiring a relative tilt of ≈–19° along the horizontal $<010>_{pc}$ perovskite direction to arrive at the Ni <111> zone axis in Figure 4f. Here a stacking fault can be seen running diagonally across the particle and along a {111} plane, shown more clearly in the inset. Due to the larger pseudocubic unit cell

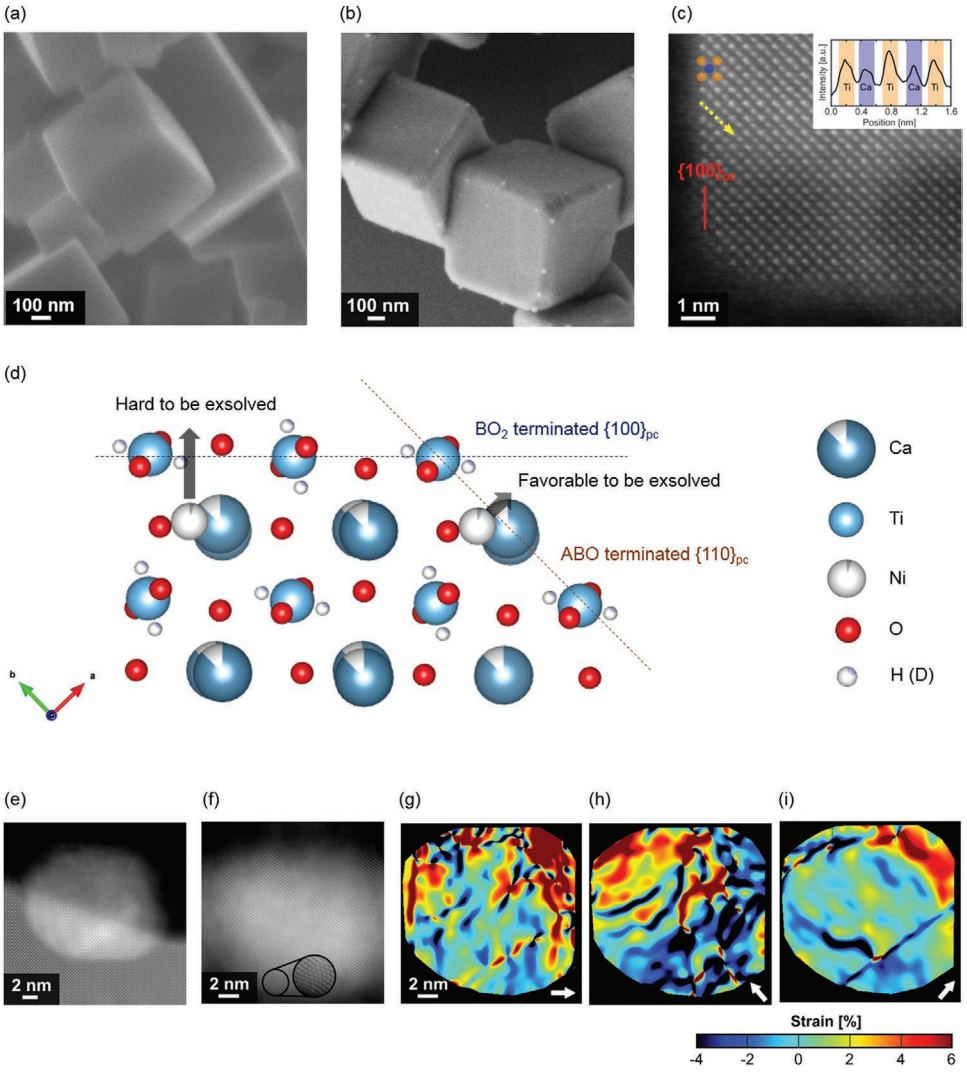

Figure 4. Ni exsolution from the A-site in CNTO(ST). a) SEM image of as-prepared CNTO(ST). b) SEM image of Ni nanoparticles (bright dots) exsolved from CNTO(ST). c) Cross-sectional HAADF image of the corner of an as-prepared CNTO(ST) cube with the inset line profile showing the B-site termination of the $\{100\}_{pc}$ facets. d) Crystal structure of the as-prepared CNTO(ST) obtained from HRPD refinement. e–i) Atomic resolution STEM images of the perovskite and Ni nanoparticles along with strain maps calculated relative to bulk Ni. The arrows correspond to the crystal axes of the strains which are g) <200> and h,i) <111>. The color bars are the same for all the strain maps. The particle is partially embedded and emerge from the $\{110\}_{pc}$ terraces. (e) is aligned to the $<001>_c$ perovskite zone axis, and (f) to the nanoparticle <110> zone axis.

of CNTO relative to Ni, the nanoparticles can be expected to be strained. Regions of enhanced tensile strain can be seen along the <111> directions in the top left and right corners of Figure 4h,i, respectively. In these regions, a maximum value of ≈5% is observed corresponding to d_{111} = 2.14 Å. Near the base of the particle where it is embedded in the perovskite, compressive strains of ≈–1.5 to –2% can be seen, which correspond to differences of ≈3–4 pm for the respective d-spacings.

Preferential {111}-termination of nanoparticles, as in Figure 4, is to be expected with fcc metals such as Ni since these are the most thermodynamically stable facets. It has previously been reported that tensile strains in transition metals can shift the d-band center and increase the strength of metal–oxygen bonds.[34] As such, the tensile strain observed around the exposed faces here may lead to improved electrochemical performance through enhanced chemisorption. Moreover, the increased interaction of metal nanoparticles with the perovskite support, especially in the case of the semi-embedded particle in Figure 4e,f, will likely improve the stability of the system.

3. Conclusion

We have prepared A-site deficient hydrated $CaTiO_3$ by direct replacement of lattice oxygens with hydroxide via solvothermal routes, obtaining higher proton concentrations and better proton conductivity than the conventional approach of B-site doping with aliovalent transition metal cations to create oxygen vacancies. The excellent hydration capability of the parent compound with the shorter O—O distances in TiO_6 octahedra leads to much

higher proton conductivity compared to stoichiometric $CaTiO_3$ prepared by solid-state method. Powder neutron diffraction and EXAFS studies reveals that unusual A-site deficient stoichiometry followed by hydration allows Ni^{2+} ions to be substituted for Ca sites with square-planar coordination. Ni nanoparticles with preferential formation of {111}-termination and tensile strain about these facets are then preferentially exsolved along pseudocubic $\{110\}_{pc}$ planes of these $CaTiO_3$ upon reduction, with strong anchorage and orientation on the perovskite surfaces.

Supporting Information

Supporting Information is available from the Wiley Online Library or from the author.

Acknowledgements

This research was supported by the UK Engineering and Physical Sciences Research Council (grant nos.: EP/R023522/1, EP/R023751/1, EP/L017008/1 and EP/P007821/1). The authors would like to thank Prof. Martin Owen Jones for useful discussions. Experiments at the ISIS Neutron and Muon Source were supported by beamtime allocation RB1920629 from the Science and Technology Facilities Council. The authors would also like to thank Diamond Light Source for beamtime (proposal SP17198-8), and the staff at beamline B18, in particular Alan Chadwick and Giannantonio Cibin, for assistance with XAS testing and data collection. Calculations were performed on the UK Archer high-performance computing (HPC) facility, via the UK Materials Chemistry Consortium, which was funded by the EPSRC (EP/L000202, EP/R029431).

Conflict of Interest

The authors declare no conflict of interest.

Data Availability Statement

The research data underpinning this publication can be accessed at https://doi.org/10.17630/5d589f15-0111-4d25-8420-963bf1cf0aed.

Keywords

defect chemistry, exsolution, hydration, perovskite, proton conductivity

Received: April 28, 2021
Revised: June 27, 2021
Published online:

[1] K. D. Kreuer, *Chem. Mater.* **1996**, *8*, 610.
[2] K. D. Kreuer, *Solid State Ionics* **1999**, *125*, 285.
[3] K. D. Kreuer, *Solid State Ionics* **2000**, *136–137*, 149.
[4] P. Norby, *Perovskite Oxide for Solid Oxide Fuel Cells. Fuel Cells and Hydrogen Energy*, (Ed: T. Ishihara), Springer, Boston, MA **2009**.
[5] H. G. Bohn, T. Schober, *J. Am. Ceram. Soc.* **2000**, *83*, 768.
[6] K. D. Kreuer, T. Dippel, Y. M. Baikov, J. Maier, *Solid State Ionics* **1996**, *86–88*, 613.
[7] K. D. Kreuer, S. T. Adams, W. Münch, A. Fuchs, U. Klock, J. Maier, *Solid State Ionics* **2001**, *145*, 295.
[8] S. Ricotea, N. Bonanos, G. Caboche, *Solid State Ionics* **2009**, *180*, 990.
[9] S. Sasaki, C. T. Prewitt, J. D. Bass, *Acta Crystallogr.* **1987**, *C43*, 1668.
[10] W. Munch, K. D. Kreuer, G. Seifertli, J. Majer, *Solid State Ionics* **1999**, *125*, 39.
[11] W. Munch, K. D. Kreuer, G. Seifertli, J. Majer, *Solid State Ionics* **2000**, *136–137*, 183.
[12] J. Irvine, D. Neagu, M. Verbraeken, C. Chatzichristodoulou, C. Graves, M. B. Mogensen, *Nat. Energy* **2016**, *1*, 15014.
[13] S. Tao, J. Irvine, *Nat. Mater.* **2003**, *2*, 320.
[14] J. Suntivich, K. J. May, H. A. Gasteiger, J. B. Goodenough, Y. Shao-Horn, *Science* **2011**, *334*, 1383.
[15] J. G. Lee, J. Hwang, H. J. Hwang, O. S. Jeon, J. Jang, O. Kwon, Y. Lee, B. Han, Y. G. Shul, *J. Am. Chem. Soc.* **2016**, *138*, 3541.
[16] W. Wang, M. O. Tadé, Z. Shao, *Chem. Soc. Rev.* **2015**, *44*, 5371.
[17] N. Sata, K. Hiramoto, M. Ishigame, S. Hosoya, N. Niimura, S. Shin, *Phys. Rev. B* **1996**, *54*, 15795.
[18] R. Waser, *J. Am. Ceram. Soc.* **1988**, *71*, 58.
[19] D. Bavykin, J. Friedrich, F. Walsh, *Adv. Mater.* **2006**, *18*, 2807.
[20] J. T. S. Irvine, D. C. Sinclair, A. R. West, *Adv. Mater.* **1990**, *2*, 132.
[21] S. Fop, K. S. McCombie, E. J. Wildman, J. M. S. Skakle, J. T. S. Irvine, P. A. Connor, C. Savaniu, C. Ritter, A. C. Mclaughlin, *Nat. Mater.* **2020**, *19*, 752.
[22] S. Yamaguchi, K. Kobayashi, T. Higuchi, S. Shin, Y. Iguchi, *Solid State Ionics* **2000**, *136–137*, 305.
[23] P. I. Dahl, R. Haugsrud, H. L. Lein, T. Grande, T. Norby, M.-A. Einarsrud, *J. Eur. Ceram. Soc.* **2007**, *27*, 4461.
[24] J. G. Lee, A. Gibbs, C. Savaniu, J. Payne, M. Jones, N. A. Naden, J. T. S. Irvine, *ISIS Neutron and Muon Source Data J.* **2019**, https://doi.org/10.5286/ISIS.E.RB1920629.
[25] F. M. Draber, C. Ader, J. P. Arnold, S. Eisele, S. Grieshammer, S. Yamaguchi, M. Martin, *Nat. Mater.* **2020**, *19*, 338.
[26] J. G. Lee, J. -H. Myung, A. B. Naden, O. S. Jeon, Y. G. Shul, J. T. S. Irvine, *Adv. Energy Mater.* **2020**, *10*, 1903693.
[27] R. D. Shannon, C. T. Prewitt, *Acta Crystallogr.* **1969**, *B25*, 925.
[28] A. M. Beale, M. Paul, G. Sankar, R. J. Oldman, C. R. A. Catlow, S. French, M. Fowles, *J. Mater. Chem.* **2009**, *19*, 4391.
[29] S. Zhang, M. B. Katz, S. Dai, K. Zhang, X. Du, G. W. Graham, X. Pan, *J. Phys. Chem. C* **2017**, *121*, 17348.
[30] D. Neagu, G. Tsekouras, D. N. Miller, H. Ménard, J. T. S. Irvine, *Nat. Chem.* **2013**, *5*, 916.
[31] D. Neagu, T. -S. Oh, D. N. Miller, H. Ménard, S. M. Bukhari, S. R. Gamble, R. J. Gorte, J. M. Vohs, J. T. S. Irvine, *Nat. Commun.* **2015**, *6*, 8120.
[32] P. Hartel, H. Rose, C. Dinges, *Ultramicroscopy* **1996**, *63*, 93.
[33] R. W. G. Wyckoff, *Crystal Structures*, 2nd ed., Interscience Publishers, New York **1963**.
[34] M. Mavrikakis, B. Hammer, J. K. Nørskov, *Phys. Rev. Lett.* **1998**, *81*, 2819.